Engineering, 2026, 18(5), 155-183
https://www.scirp.org/journal/eng
ISSN Online: 1947-394X
ISSN Print: 1947-3931

Study of Injection Rate on Fracture Network Complexity during Hydraulic Fracturing: Experimental Insights from Concrete, Sandstone and Bituminous Coal

Tresphord Chishimba[1,2*], Weiguo Liang[1,2*], Ngambua Ngambua Rene[1,2,3], Irfan Ahmad Butt[1,2]

[1]College of Mining Engineering, Taiyuan University of Technology, Taiyuan, China
[2]Key Laboratory of *In-Situ* Property Improving Mining of Ministry of Education, Taiyuan University of Technology, Taiyuan, China
[3]Faculty of Oil, Gas and New Energies, University of Kinshasa, Kinshasa, DRC
Email: *liangweiguo@tyut.edu.cn, *treschishimba@gmail.com

How to cite this paper: Chishimba, T., Liang, W.G., Rene, N.N. and Butt, I.A. (2026) Study of Injection Rate on Fracture Network Complexity during Hydraulic Fracturing: Experimental Insights from Concrete, Sandstone and Bituminous Coal. *Engineering*, **18**, 155-183.
https://doi.org/10.4236/eng.2026.185011

Received: March 11, 2026
Accepted: May 5, 2026
Published: May 8, 2026

Abstract

This study examines the influence of injection rate on fracture development during hydraulic fracturing using water as the fracturing fluid. Laboratory experiments were performed on concrete, low-permeability sandstone, and brittle bituminous coal over a broad range of injection rates. The results indicate that both low (<1.0 mL/min) and high (≥5.0 mL/min) injection rates predominantly produced simple, planar fractures, reflecting limited fracture branching. In contrast, an intermediate injection rate of 2.2 mL/min consistently resulted in the most complex fracture patterns. The potential for enhanced fracture complexity was inferred from fracture surface roughness obtained via 3D scanning and characterized using the Joint Roughness Coefficient (JRC), which exhibited its highest values at this intermediate injection rate. Although water is sometimes considered less effective than unconventional fluids, the findings demonstrate that it performs well in moderately permeable rocks with sufficient tensile strength. However, water was less effective in brittle coal and low-permeability sandstone, where more compressible, low-viscosity fluids may be advantageous. Overall, three fracture behavior regimes were identified: a low-rate regime producing simple fractures, a mid-rate optimal regime producing complex networks, and a high-rate regime where fracture complexity decreased. Building on earlier findings that associate higher fluid injection rates with increased fracture complexity, this study explicitly identifies a limiting injection rate beyond which fracture network complexity no longer exhibits significant growth. Thin fractures dominated because controlled injection conditions focused on observing fracture behavior rather than merely inducing fracture, as reflected by the relatively high post-fracture injection pressure.

Keywords

Hydraulic Fracturing, Injection Rate, Fracture Propagation, Fluid Viscosity, Fracture Complexity

1. Introduction

This hydraulic fracturing performance is critically dependent on the complexity and connectivity of the induced fracture network, which directly influences reservoir productivity in applications ranging from hydrocarbon recovery to geothermal energy, CO_2 sequestration, and hydrogen storage [1] [2]. The lack of a systematic, formation-specific understanding of how injection rate influences fracture initiation and propagation hinders the ability to optimize fracture network complexity, surface area, and connectivity. Current knowledge is further limited by the nonlinear interactions between injection rate and geo-mechanical conditions, which can lead to unpredictable outcomes in both laboratory and field-scale operations. This highlights the need for controlled experimental, theoretical, and numerical studies to establish optimal injection rates that maximize fracture complexity while avoiding undesirable effects such as premature fracture crossing, excessive vertical growth, or reduced network connectivity.

Hydraulic fracturing has emerged as a transformative engineering technique for enhancing the productivity of low-permeability geological formations. By injecting pressurized fluid into subsurface rock, this method induces the initiation and propagation of fractures, creating artificial pathways that significantly improve fluid flow. The effectiveness of hydraulic fracturing depends not merely on the initiation of fractures but also on the complexity and interconnectivity of the resulting fracture networks. It is within this context that operational parameters, especially injection rate and fluid viscosity, assume critical importance in dictating the geometry and efficacy of induced fractures [3]-[6].

Fracture complexity is a multifaceted outcome that encompasses the number, orientation, branching behavior, and interaction of fractures within a given rock volume. Complex fracture networks are crucial because they increase the contact area between the fluid and the rock matrix, thereby enhancing hydrocarbon extraction and thermal exchange in geothermal applications. Achieving such complexity is contingent upon a delicate balance between various geological, mechanical, and operational factors. Among these, the rate at which fluid is injected and the physical properties of the fluid itself, most notably viscosity, are two of the most controllable and influential parameters. Understanding how these two factors interact to govern the evolution of fracture networks is crucial for optimizing hydraulic fracturing processes across a wide range of geological settings [7].

The injection rate, defined as the volume of fluid introduced into the formation per unit time, determines the rate of energy delivery into the subsurface [8] [9]. A higher injection rate can lead to rapid pressurization, triggering dynamic fracture propagation and potentially promoting fracture branching or bifurcation. Conversely, a low injection rate may result in delayed or incomplete fracture initiation, with fluid infiltration dominating over fracture propagation. However, a simplistic interpretation of injection rate effects can be misleading. For instance, excessively high rates may cause premature fracture crossing through existing natural fractures or bedding planes, reducing fracture complexity and increasing the risk of vertical growth beyond the target zone. Thus, there exists an optimal window of injection rate that must be identified and tailored to the geo-mechanical characteristics of the target formation.

Fracture propagation in rock is governed by principles from fracture mechanics, particularly the concepts of stress intensity factors [10] and energy release rates [11] [12]. According to mode I fracture theory, propagation occurs when the stress intensity at the crack tip exceeds the material's fracture toughness. The rate of pressurization, controlled by injection rate and viscosity, determines how quickly this threshold is reached. Furthermore, energy-based models suggest that crack propagation is energetically favorable when the strain energy release rate exceeds the energy required to create new surfaces. Since both injection rate and viscosity influence the accumulation and dissipation of strain energy, their effect on fracture initiation and growth is both direct and profound. In heterogeneous or naturally fractured rock masses, the situation becomes more complex. Natural fractures [13]-[16], bedding planes, and faults interact with hydraulic fractures in unpredictable ways [17] [18]. The nature of this interaction, whether the hydraulic fracture crosses, offsets, or is deflected by a natural fracture, depends on several factors, including the angle of approach, the mechanical contrast across the interface, and the characteristics of the fluid injection. The injection rate and fluid viscosity can modulate this interaction by altering the local stress field and pressure gradients at the point of intersection. For example, a high injection rate may allow a hydraulic fracture to cross a natural fracture due to inertia, whereas a lower rate might promote deflection and thereby enhance the fracture's complexity. These nuanced behaviors underscore the need for an integrated experimental and theoretical approach to understand fracture-fluid interactions.

Several studies have attempted to empirically relate injection parameters to fracture behavior [19]-[21]. Laboratory experiments using synthetic rock analogs, real rock specimens, and advanced monitoring systems such as acoustic emission sensors and high-speed cameras have provided valuable insights into the time evolution of fracture networks [22]. These investigations suggest that optimal injection strategies must be adapted to the specific fluid-rock system under consideration [23]. Modern numerical simulations using discrete element methods and coupled hydro-mechanical models have reinforced the view that the interaction between injection rate and viscosity is neither trivial nor universally predictable, but is instead formation-dependent and highly sensitive to in-situ conditions [24] [25].

In practical applications, field-scale hydraulic fracturing operations face additional constraints, such as equipment limitations, economic considerations, and environmental regulations. The optimization of injection protocols must therefore balance operational feasibility with geo-mechanical effectiveness.

Given the centrality of fracture network complexity to production performance and reservoir sustainability, there is a pressing need to develop a systematic understanding of how injection rate governs fracture initiation, propagation, and network development under controlled fluid conditions. The goal is not only to maximize fracture surface area but also to enhance fracture connectivity and conductivity, thereby improving the long-term efficiency of resource extraction. This requires a comprehensive research approach that involves controlled laboratory tests, theoretical modeling, and, where feasible, pilot-scale field trials.

This paper aims to investigate the influence of injection rate on fracture branching behavior in representative rock materials. The experiments are conducted under conditions that mimic *in-situ* stress states, with water as the fracturing fluid to maintain consistent fluid properties. By systematically varying the injection rate, the study isolates its role in fracture initiation, propagation paths, and resulting fracture network complexity. The results are expected to contribute to the development of refined hydraulic fracturing strategies that are efficient and aligned with the geo-mechanical characteristics of diverse geological formations.

2. Methodology and Sample Preparation

2.1. Sample Preparation

2.1.1. Concrete Preparation

A 42.5 MPa (42.5 N/mm^2) cement type, sand, and water were mixed in a ratio of 1:1:0.4 [26] [27] by weight, respectively (e.g., the weight of cement was 7.5 kg, the same as the weight of sand and water, which was 3 kg). To achieve a uniform grain size for the sand, sieving was performed using a 30-mesh sieve, equivalent to 0.6 mm, as shown in **Figure 1**. Additionally, weighed cement, sand, and water were placed in a bucket and stirred thoroughly to obtain a uniform mixture. The mixture was then poured into cubic molds measuring 100 × 100 × 100 mm to cast the concrete. The mixture was also poured into cylindrical molds measuring 100 mm and 50 mm in length and diameter, respectively, according to the recommended International Standard for Rock Mechanics (ISRM) for testing Uniaxial Compressive Strength (UCS) [28]. This was to later check the quality of the concrete. The concrete mix was then left to cure for the recommended period of 28 days in a location away from sunlight to achieve maximum strength [29]. See **Figure 1** below:

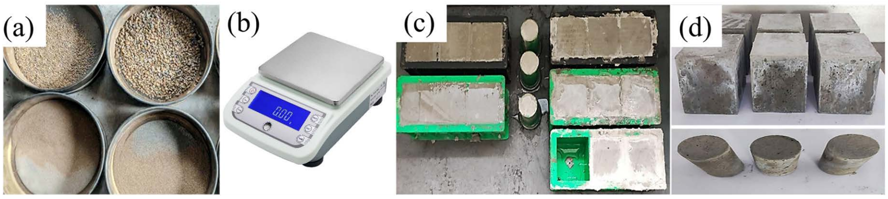

Figure 1. Concrete preparation (a) size 30 mesh and sieved sand, (b) electronic weighing scale, (c) wet concrete mix, (d) dried concrete.

To maintain the concrete's hydration during the curing period, water was continuously added to it over the first twelve days to achieve maximum strength [30]. The uniaxial compressive strength test results for concrete are presented in **Figure 2** and **Table 1**. For accurate results, the test was conducted at a loading rate of 0.100 mm/min [31].

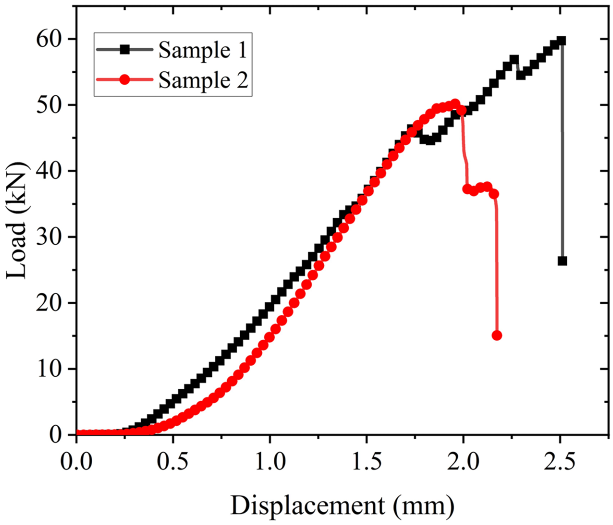

Figure 2. Concrete UCS test results from two samples.

Table 1. UCS results.

Sample	*A*	*B*	*Average* (*A & B*)	*Standard*
UCS value (MPa)	30.43	25.56	28	20 - 50

The calculated average UCS value was 28 MPa, which falls within the range of standard concrete after a 28-day curing time.

2.1.2. Sandstone and Coal Preparation

In this study, in addition to concrete samples, bituminous coal and sandstone (**Figure 3**) were selected as representative rock materials due to their contrasting mechanical and permeability characteristics, which are relevant for simulating heterogeneous subsurface conditions. Each sample was precisely shaped into a cubic form with dimensions of 100 × 100 × 100 mm using a high-precision wire cutting machine. This method ensured minimal surface damage and maintained the integrity of the internal structure, which is critical for accurately capturing fracture initiation and propagation behavior under controlled laboratory conditions. The use of standardized dimensions and uniform preparation techniques facilitated repeatability and comparability across different experimental runs.

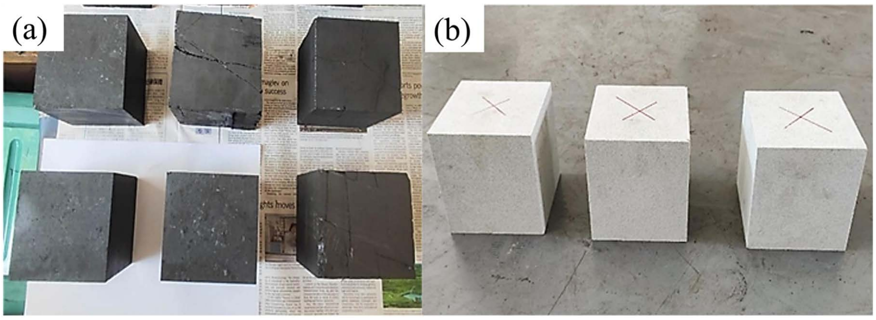

Figure 3. Natural rock samples (a) 100 × 100 × 100 mm coal samples and (b) 100 × 100 × 100 mm sandstone samples.

2.1.3. Sample Design

The samples were prepared according to the specified dimensions to facilitate the installation of the fluid injection system, ensuring a 5 mm fluid injection column was maintained, as illustrated in **Figure 4(a)**. A central borehole was drilled to a depth of 52.5 mm using a 6 mm diameter drill bit, after which compressed air was employed to remove residual drill cuttings. A steel injection pipe was then inserted into the borehole to a depth of 47.5 mm, secured with sealing tape wrapped around its lower end, thereby leaving a 5 mm space between the bottom of the hole and the pipe tip to serve as the fluid injection column. To prevent leakage during fluid injection, Epoxy resin AB glue was applied to fill the annular gap between the borehole wall and the injection pipe. This procedure was replicated for all remaining samples. The adhesive was allowed to cure for a minimum of 48 hours in accordance with the manufacturer's guidelines, prior to the commencement of the hydraulic fracturing tests. **Figure 4(b)-(d)** presents the completed sample preparation with the steel injection pipes (outside diameter = 3 mm and internal diameter = 0.5 mm) inserted.

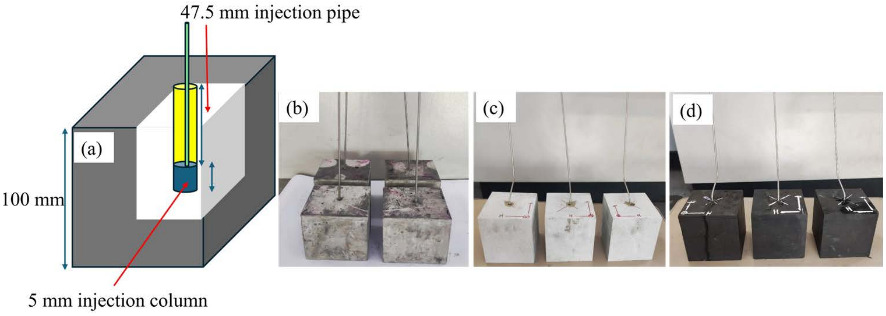

Figure 4. Prepared samples (a) sample design, (b) concrete, (c) sandstone, (d) coal.

2.2. Experimental Set-Up

The main hydraulic fracturing equipment was the HADZ-IV true tri-axial seepage hydraulic fracturing machine. It's fitted with a control unit for setting the confining stresses that mimic field conditions, *i.e.*, vertical or overburden stress (σ_v), minimum principal stress (σ_h), and maximum principal stress (σ_H) through the hydraulic-operated platens. In addition, we had a HAG-70P fluid injection pump, a central computer for data display, capture, and setting. Acoustic emission (AE) monitoring was conducted using broadband piezoelectric sensors mounted symmetrically on the specimen surface. Prior to sensor installation, the contact areas were cleaned and smoothed to ensure optimal acoustic coupling. A thin layer of coupling agent (Gel) was applied between each sensor and the specimen, and the sensors were mechanically secured to maintain stable contact. The AE signals were amplified using 40 dB pre-amplifiers (adjustable range 0 - 100 dB). A detection threshold of 40 dB was selected based on preliminary noise tests to suppress background mechanical interference while ensuring reliable detection of microcrack-induced AE events.

Figure 5 below shows the main equipment, and Figure 6 shows its corresponding schematic diagram.

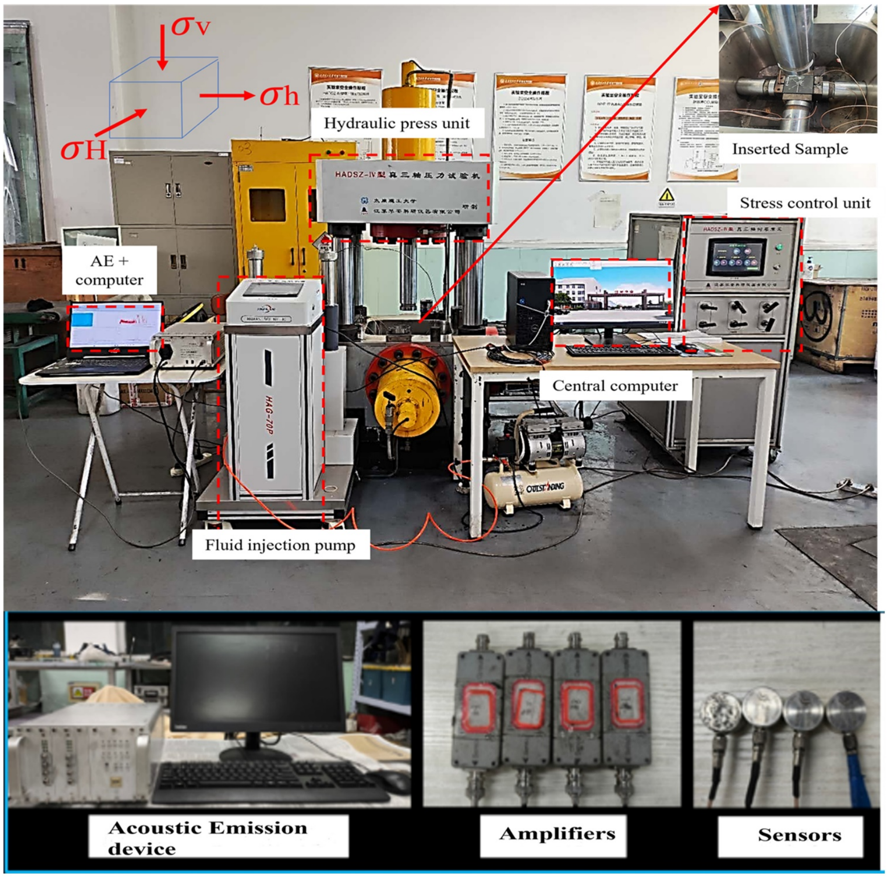

Figure 5. Main equipment of the hydraulic fracturing test.

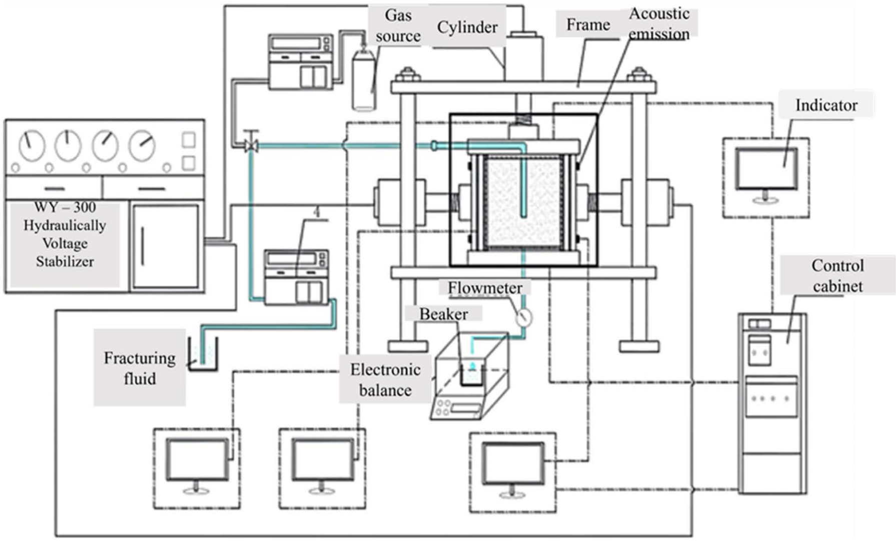

Figure 6. Schematic diagram of the hydraulic fracturing test.

Table 2. Experimental conditions.

Test No.	Q (mL/min)	*In-situ* stresses (MPa)		
		σ_v	σ_H	σ_h
C1	2.0	25	20	15
C2	8.0	25	20	15
C3	0.2	25	20	15
C4	2.0	25	20	15
C5	8.0	25	20	15
C6	0.6	25	20	15
C7	8.0	25	20	15
C8	20.0	25	20	15
C9	5.0	25	20	15
C10	1.8	25	20	15
C11	2.2	25	20	15
C12	2.2	25	20	15
SST13	2.2	25	20	15
Coal14	2.2	12	8	5
Coal15	1.0	12	8	5

The fracturing fluid used in the experiment was water at room temperature (around 20˚C to 25˚C) and atmospheric pressure (1 atm), and the assumed depth for the fracture test was set at 1000 m. Different injection rates, ranging from as low as 0.2 mL/min to 20 mL/min, were applied while observing the results. With the density of sandstone taken as 2500 kg/m^3, the vertical stress was calculated to be 25 MPa, and a normal faulting condition ($\sigma_v > \sigma_H > \sigma_h$) was used to determine the values for the minimum and maximum principal stresses as 15 MPa and 20 MPa, respectively. Since standard concrete can have a density (2200 - 2500 kg/m^3) [32] similar to that of sandstone, the same values for in-situ stresses were used for concrete samples. However, bituminous coal with a much lower density, taken as 1200 kg/m^3 [33] for this test at the same depth, its overburden stress was calculated as 12 MPa, and it was equally assumed that a normal faulting condition would prevail to set the minimum and maximum principal stresses similarly as 5 MPa and 8 MPa, respectively. Table 2 above summarizes the laboratory set conditions for all the tests. In the table, C1 refers to test numbers 1 through 14 on a concrete sample, SST13 as test number 13 on a sandstone sample, and coal14 and coal15 as test numbers on coal samples.

3. Results and Discussion

In this section, the results of hydraulic fracturing tests using concrete, sandstone, and coal samples with varying injection rates are presented. Specifically, the fracture behaviors in different rocks, the injection rate conditions for fractures to penetrate various rocks, and the fracture surfaces are discussed.

3.1. Hydraulic Fracture (HF) Behavior at Different Injection Rates

In general, the hydraulic fractures propagated perpendicular to the minimum principal stress (σ_h), consistent with the theoretical prediction of Mode I fracture opening under high fluid pressure. Samples such as C1, C2, C3, C4, C5, C6, and C7 (Figures 7-9) exhibited well-defined, planar fracture surfaces with minimal deviation or branching, indicating a stable fracture growth mechanism. These results suggest that, within a certain range of injection rates, fracture propagation is predominantly controlled by the stress field and rock matrix properties, with a limited influence from pre-existing heterogeneities. C1, conducted at a rate of 2.0 mL/min, showed planar fracture surfaces, while C4, conducted at the same rate, showed some irregularities in the fracture surface. Tests with high injection rates, such as C2 and C5, exhibited a planar fracture surface, similar to those observed at low rates in the case of C3.

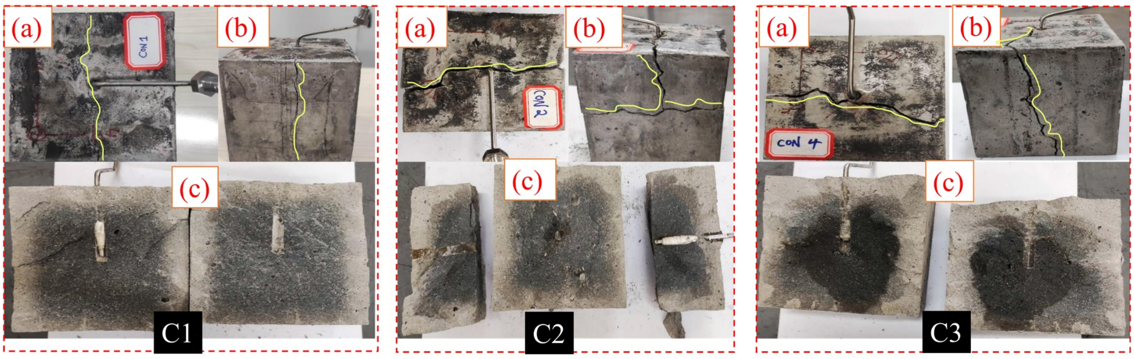

Figure 7. Tested samples C1 (a) HF direction, (b) HF development, (c) fracture surface; C2 (a) HF direction, (b) HF development, (c) HF surface; C3 (a) HF direction, (b) HF development, (c) HF surface.

As injection rates increased (up to 20 mL/min), fracture propagation remained efficient and planar, consistent with sufficient pressure buildup overcoming tensile strength and cohesive forces along the weakest plane perpendicular to σ_h. Conversely, tests conducted at low injection rates (e.g., <0.2 mL/min) failed to initiate fractures, indicating that below a critical pressure threshold, the induced fluid pressure is insufficient to exceed the breakdown pressure of the rock matrix or overcome the confining stress. In samples like C6 and C8 (Figure 9 and Figure 12), the resulting fracture surfaces remained relatively smooth and uniform, suggesting minimal energy dissipation during infiltration, limiting multiple fracture initiation points and the consequential branching.

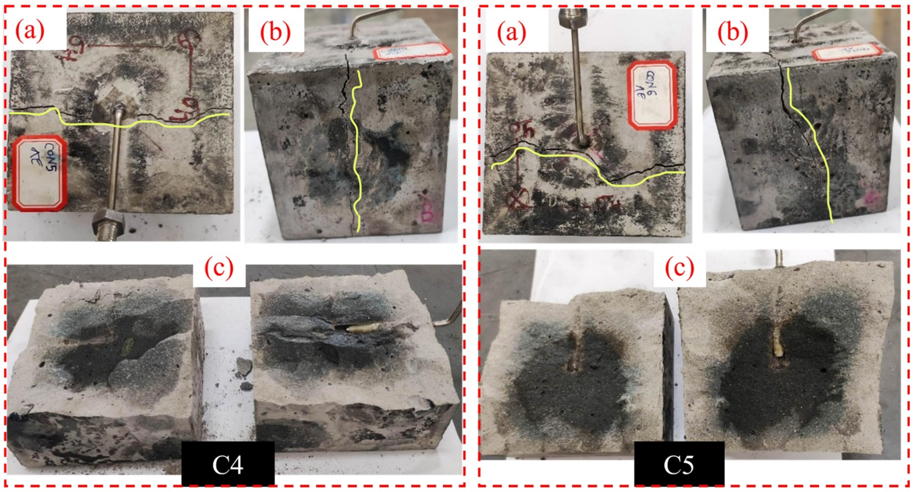

Figure 8. Tested samples C4 (a) HF direction, (b) HF development, (c) fracture surface; C5 (a) HF direction, (b) HF development, (c) fracture surface.

In contrast, more complex fracture behaviors were observed in samples that allowed a longer fluid infiltration time, accompanied by acoustic emission (AE) signal detection, for example, in C11. Similarly, C12 exhibited multiple thin fractures originating from the base and lateral sections of the sample, indicating that the stress distribution and fracture energy were redistributed upon encountering pre-existing features, as shown in Figure 11. These irregular patterns suggest the initiation of secondary fractures or branching. This emphasizes the importance of internal structural mapping, where CT scanning can provide crucial insights into internal fracture intersections and hidden discontinuities that influence fracture geometry. In Coal14, as shown in Figure 13, HF propagation was significantly inhibited or deviated due to interaction with pre-existing discontinuities. The inability of the fracture to cross a natural fracture in Coal14, likely due to a wide-aperture natural fracture acting as a barrier, resulted in fracture termination or deviation. Figure 13 also shows a planar fracture surface from a test conducted on sandstone; fracture complexity could not be attained due to the poor infiltration process in a highly impermeable rock type.

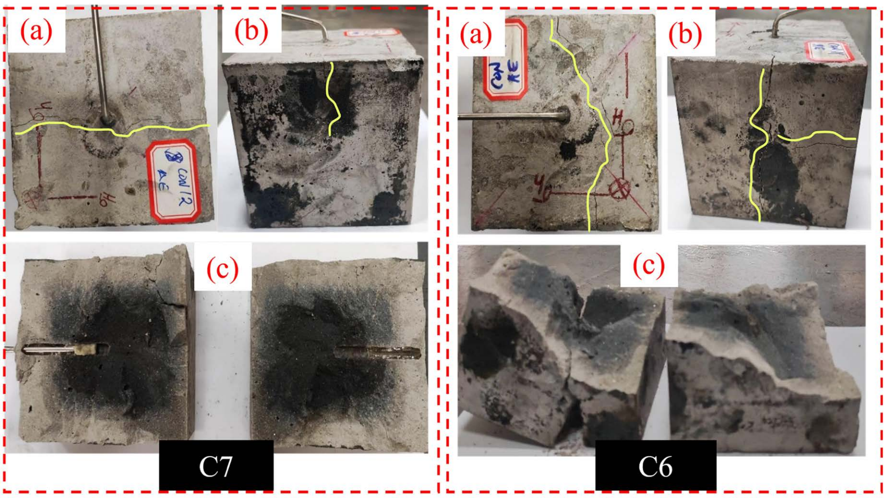

Figure 9. Tested samples C7 (a) HF direction, (b) HF development, (c) fracture surface; C6 (a) HF direction, (b) HF development, (c) fracture surface.

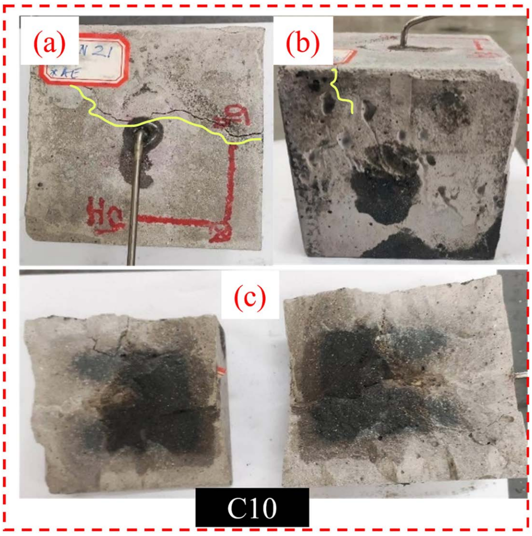

Figure 10. Tested sample C10 (a) HF direction, (b) HF development, (c) fracture surface.

One of the most significant findings emerged from sample Coal15 (**Figure 14**), where an injection rate of 1.0 ml/min failed to generate a conventional hydraulic fracture. Instead, fluid pressure exploited an existing natural fracture aligned with the injection column, resulting in failure along that plane rather than initiating a new HF. This demonstrates that the presence of natural fractures intersecting the injection column can drastically alter the fracturing process by providing a preferential flow path, thereby relieving pressure and preventing new fracture initiation. **Figure 10** illustrates a transition in which the results gradually improved as the injection rate increased from a very low to a medium rate, with fracture surfaces exhibiting minor irregularities. Test sample C9, conducted at a rate of 5.0 mL/min, yielded a reversal of results compared to the planar fracture surface. To emphasize the poor results as the injection rate increased, C8 was conducted at 20 mL/min, yielding a similar flat fracture surface. Both of these results are shown in Figure 12.

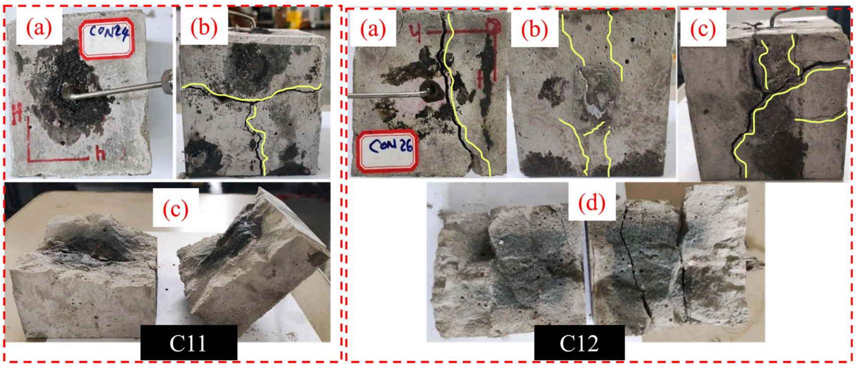

Figure 11. Tested samples C11 (a) HF direction, (b) HF development, (c) fracture surface; C12 (a) HF direction, (b) multiple HF development, (c) fracture development, (d) fracture surface.

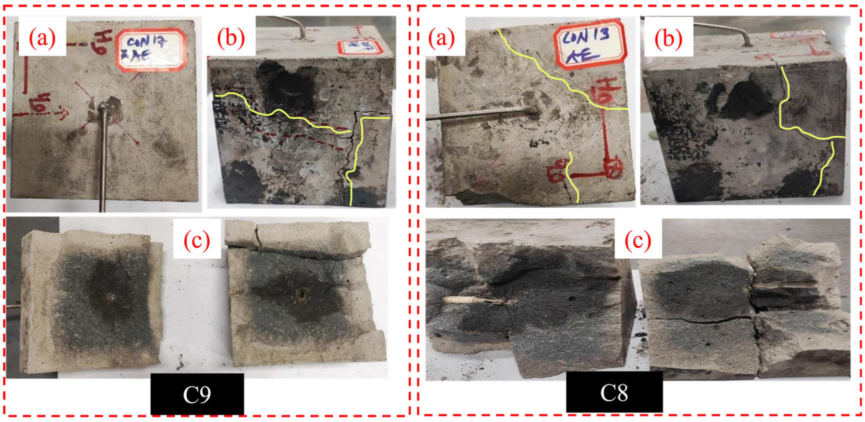

Figure 12. Tested samples C9 (a) HF direction, (b) HF development, (c) fracture surface; C8 (a) HF direction, (b) HF development, (c) fracture surface.

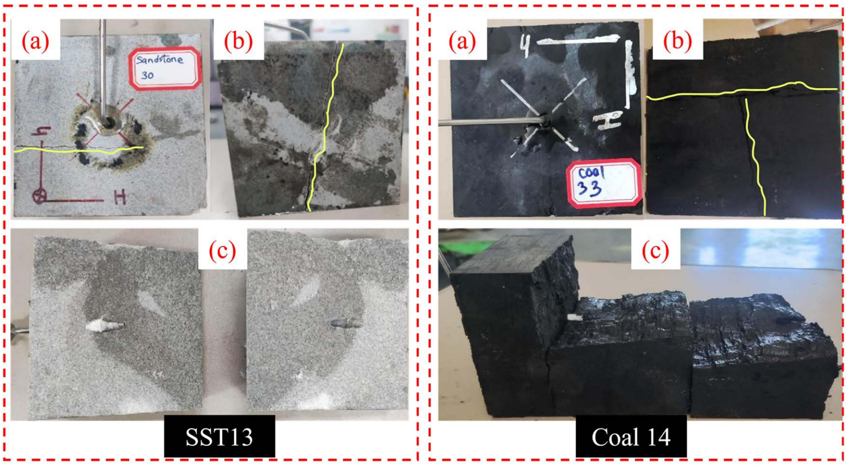

Figure 13. Tested samples SST13 (a) HF direction, (b) HF development, (c) fracture surface; Coal14 (a) HF direction, (b) HF development, (c) fracture surface.

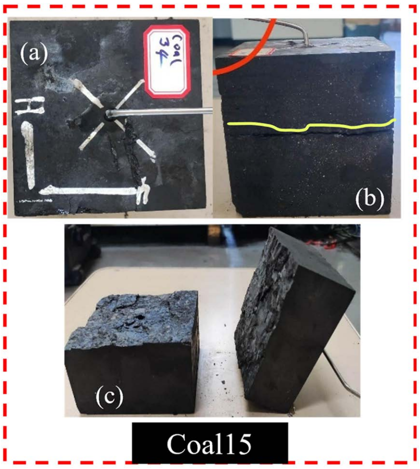

Figure 14. Tested sample Coal15 No HF development.

3.2. Injection Pressure Evolution

Figure 15 illustrates the injection pressure-time evolution for samples C1, C2, and C3, highlighting the effects of varying injection rates on fracture initiation and pressure response. In test C1, conducted at an injection rate of 2.0 mL/min, fracture initiation occurred at a breakdown pressure of 30.44 MPa after 149 seconds and 4.96 mL of water injection. The breakdown event was followed by a brief pressure plateau lasting approximately 8 seconds, after which the pressure declined slightly to 30.16 MPa and subsequently to 27.16 MPa, indicating the onset of fluid infiltration into the created fracture. A notable pressure recovery phase occurred after 15 seconds, stabilizing at an average of 27.7 MPa. This recovery is indicative of progressive fracture opening and sealing behavior, possibly influenced by minor fluid leakage or partial fracture closure. The absence of additional breakdown events suggests that the initial fracture pathway remained dominant throughout the test, with high residual pressure supporting the presence of thin but hydraulically conductive fractures.

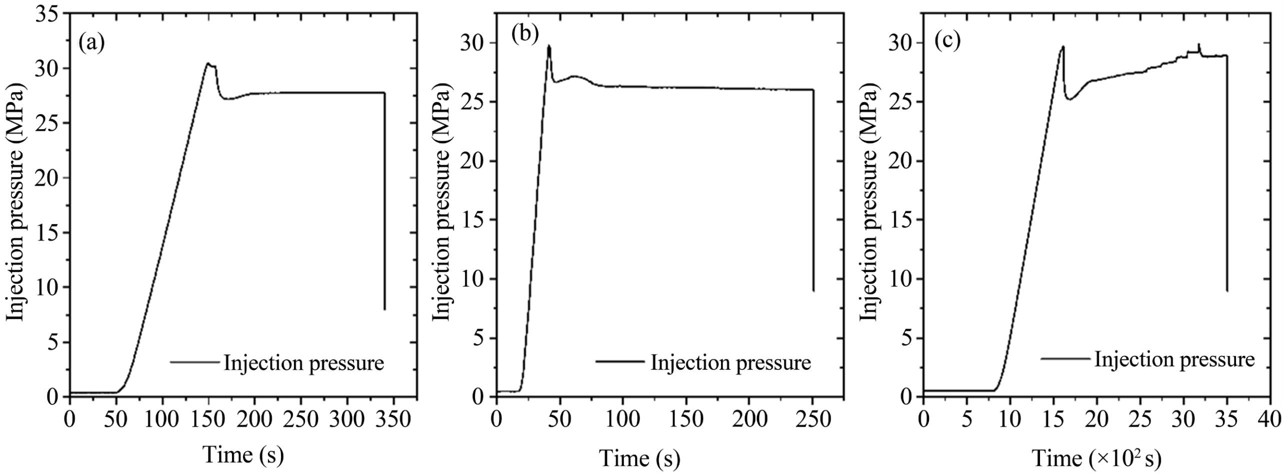

Figure 15. Pressure-time graph (a) C1, (b) C2 and (c) C3.

In contrast, test C2 was conducted at a significantly higher injection rate of 8.0 mL/min and exhibited a more abrupt pressure response. Breakdown occurred at 29.82 MPa after injecting 7.68 mL of fluid over just 41 seconds. Following the peak, pressure dropped sharply to 26.67 MPa within 5 seconds, then stabilized at an average of 26.1 MPa. The rapid pressure decay and subsequent stabilization indicate the formation of a single dominant fracture with reduced resistance to fluid flow, enabling efficient pressure dissipation. Notably, the absence of further pressure peaks suggests a stable fracture path with minimal branching. Interestingly, test C3, conducted at the lowest injection rate of 0.2 mL/min, still induced fracture initiation at a breakdown pressure of 29.68 MPa after 1612 seconds and 4.33 mL of injection. Although the peak pressure was sustained for only 3 seconds before falling to 25.21 MPa over 76 seconds, the pressure eventually recovered to 27.68 MPa. This test demonstrates that even at low injection rates, pressure can accumulate sufficiently over time to exceed the tensile strength of the rock and induce fracturing. The long duration to breakdown reflects a slow but steady pressurization process, consistent with low-rate diffusion-controlled stress buildup. However, it is worth noting that the resulting fracture network from this test was relatively simple.

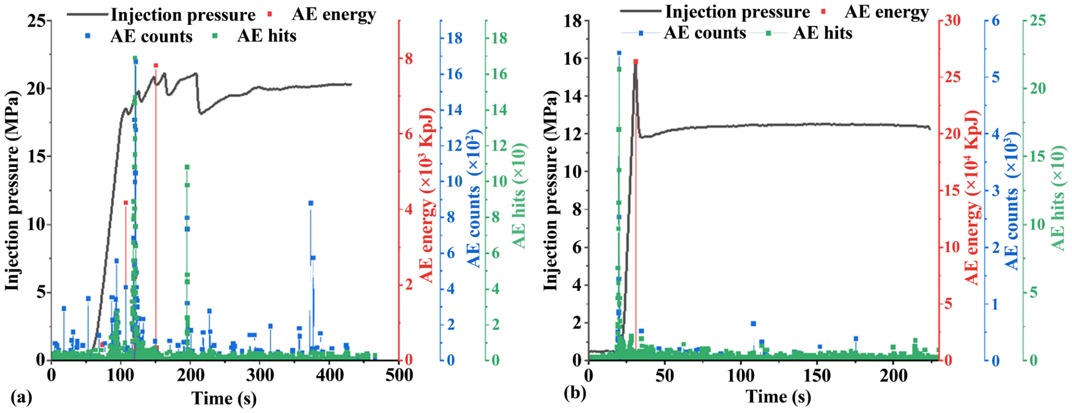

Figure 16. Pressure-time graph (a) C4, (b) C5.

Figure 16 illustrates the pressure evolution and acoustic emission (AE) activity during test C4, conducted at a flow rate of 2.0 mL/min. A breakdown occurred at a relatively low pressure of 18.51 MPa after injecting 3.38 mL of fluid over 107 seconds. Unlike the previous tests, multiple breakdown events were observed, each followed by a pressure recovery phase, with the final breakdown peak reaching 21.05 MPa. This complex pressure behavior suggests the initiation of multiple fracture tips or reactivation of pre-existing microfractures. The pressure dropped to 18.14 MPa within 7 seconds before stabilizing at a post-peak average of 19.79 MPa. Importantly, AE monitoring—recording energy, count, and hit data—was implemented during this test, offering critical insight into micro-fracturing behavior preceding macroscopic failure. Elevated AE activity prior to and during breakdown events indicates active rock damage accumulation and distributed microcrack formation. The synchronization of AE energy surges with pressure spikes strongly supports the hypothesis that micro-fracturing plays a key role in creating multiple fracture initiation sites. This phenomenon, when combined with an optimized injection rate, promotes the formation of complex fracture networks that are essential for enhancing permeability in hydraulic stimulation applications. C5, conducted at a high injection rate of 8.0 mL/min, where 2.95 mL of fluid was injected over a brief period of 31 seconds. A breakdown occurred at 15.89 MPa, with the peak pressure lasting only 1 second before rapidly dropping to 11.84 MPa within 3 seconds, and then stabilizing at an average pressure of 12.38 MPa. The extremely short pressurization window limited the rock's ability to undergo progressive micro-damage, reflected in the minimal AE activity recorded during the test. This suggests that at high injection rates, the induced pressure surpasses the tensile strength abruptly, initiating a single dominant fracture while bypassing the necessary stress redistribution phase required for multi-fracture nucleation. Thus, while fracture initiation is successful, the potential for forming a complex fracture network is significantly reduced under such rapid pressurization.

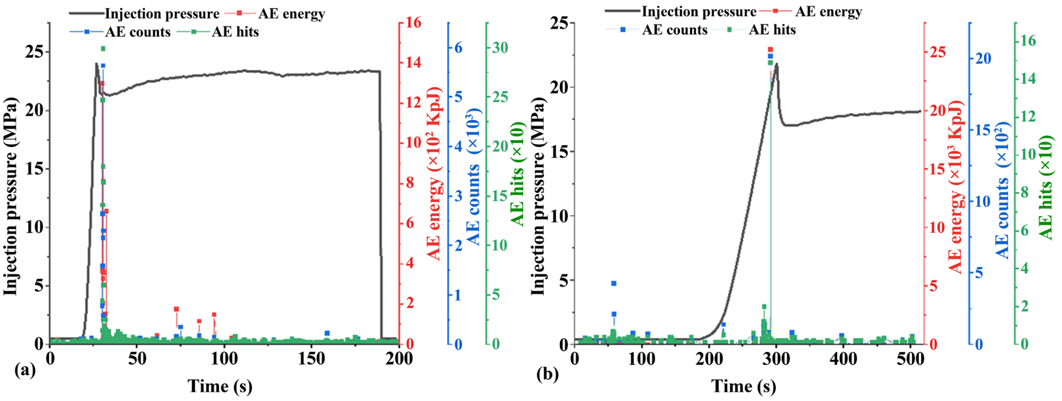

Figure 17. Pressure-time graph (a) C7 and (b) C6.

In **Figure 17**, test C7, conducted at the same rate of 8.0 mL/min, reinforces the above observations. A total of 2.55 mL was injected over 27 seconds, resulting in a breakdown pressure of 24.01 MPa. Post-breakdown, pressure declined to 21.32 MPa over 7 seconds, then stabilized at 21.69 MPa. As with C5, acoustic emission signals were negligible, indicating insufficient micro-fracturing. Conversely, test C6, performed at a much lower rate of 0.6 mL/min, involved the injection of 2.72 mL over 301 seconds, resulting in a breakdown at 21.80 MPa. Despite this extended pressurization time, the post-breakdown pressure dropped to 17.00 MPa and stabilized at 17.80 MPa. Yet, AE monitoring again recorded only limited activity, suggesting that at very low injection rates, pressure increases too gradually to generate widespread stress concentration and fails to initiate sufficient micro-fractures. Together, these tests highlight that both very high and very low injection rates are suboptimal for complex fracture development, as they either bypass or under-stimulate microcrack propagation mechanisms.

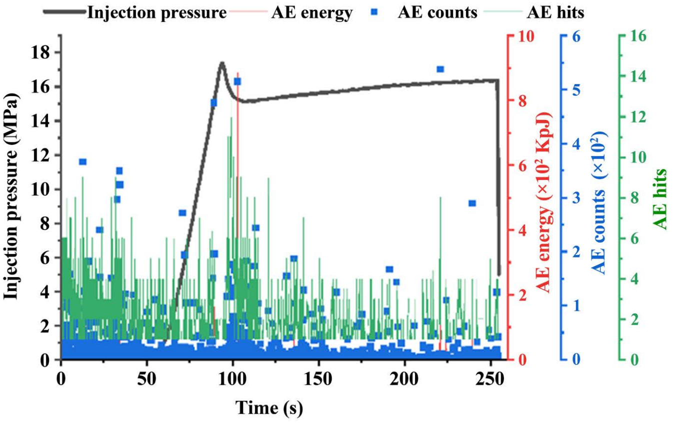

Figure 18. Pressure-time graph C10.

Figure 18 explores the transitional regime through a series of tests conducted at intermediate injection rates (1.0 - 1.9 mL/min). These tests revealed a gradual increase in injection time preceding breakdown, accompanied by a corresponding enhancement in AE signals, particularly in terms of counts and hits. Among them, test C10, at a rate of 1.8 mL/min, serves as a representative case. Breakdown occurred at 17.4 MPa after 94 seconds of injection (2.67 mL of fluid). The peak pressure lasted for 1 second, declined to 15.12 MPa within 14 seconds, and stabilized at 15.95 MPa. Throughout the injection, AE monitoring recorded consistent hit and count activity, indicating sustained micro-fracturing. However, energy levels remained low, suggesting that while distributed damage occurred, the intensity of individual fracture events was limited. These observations place C10 within a transitional fracturing regime, where fracture complexity begins to emerge but remains sub-optimal in terms of connectivity and aperture.

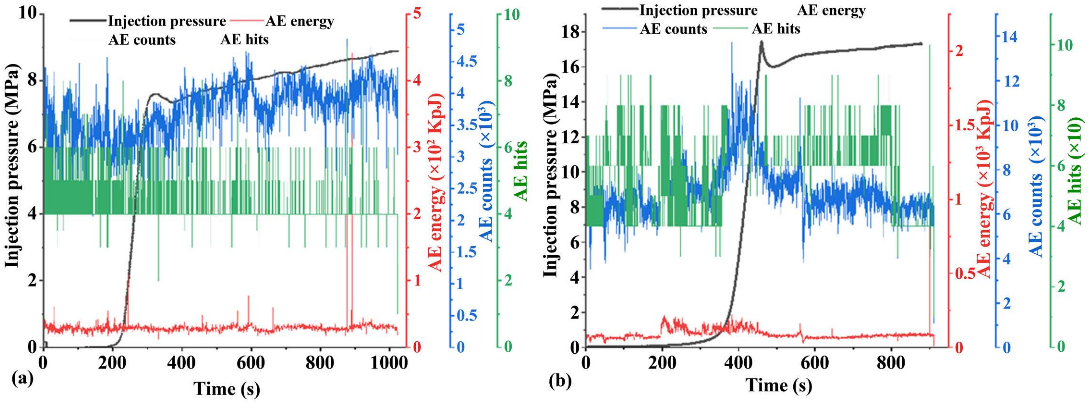

Figure 19. Pressure-time graph (a) C11 and (b) C12.

To further investigate the effectiveness of injection rates near the upper intermediate range, Figure 19 presents tests C11 and C12, both conducted at 2.2 mL/min, a slight increase from the previously tested 2.0 mL/min. In test C11, 11.48 mL of fluid was injected over 319 seconds, resulting in a breakdown pressure of 7.61

MPa. The peak was sustained for 9 seconds, followed by a drop to 7.35 MPa, and a gradual rise to an average of 8.22 MPa. Although the post-breakdown pressure increase was too gradual to trigger another failure, AE activity was high and sustained, with strong signals in hits, counts, and notably in energy levels. These elevated AE responses suggest extensive micro-damage and multiple fracture initiation points, a prerequisite for the development of complex and branched fracture networks. The absence of further breakdown despite the pressure rise implies that thin or partially open fractures created sufficient flow paths to dissipate pressure, thus preventing additional macro-fracture formation.

Also detailed in Figure 19, test C12 showed similar behavior to C11. Conducted under the same rate of 2.2 mL/min, C12 reached a breakdown pressure of 17.44 MPa after a total injection of 16.86 mL over 460 seconds. The peak pressure lasted briefly for 1 second, dropped to 16.00 MPa within 29 seconds, and then stabilized at an average of 16.86 MPa. The AE response was notably active throughout the test, with high energy levels indicating significant micro-fracture development. Despite the short duration of peak pressure, the fracture complexity inferred from AE activity aligns well with the study's objectives. C12 therefore corroborates the findings of C11, confirming that 2.2 mL/min represents an optimal injection rate for inducing complex fracture networks. This rate allows for sufficient pressurization time to stimulate micro-fractures while avoiding the abruptness of high-rate injections and the under-stimulation seen at low rates. The combination of AE signal intensity, pressure recovery behavior, and fracture response highlights the critical role of injection rate in governing fracture complexity in anisotropic geomaterials.

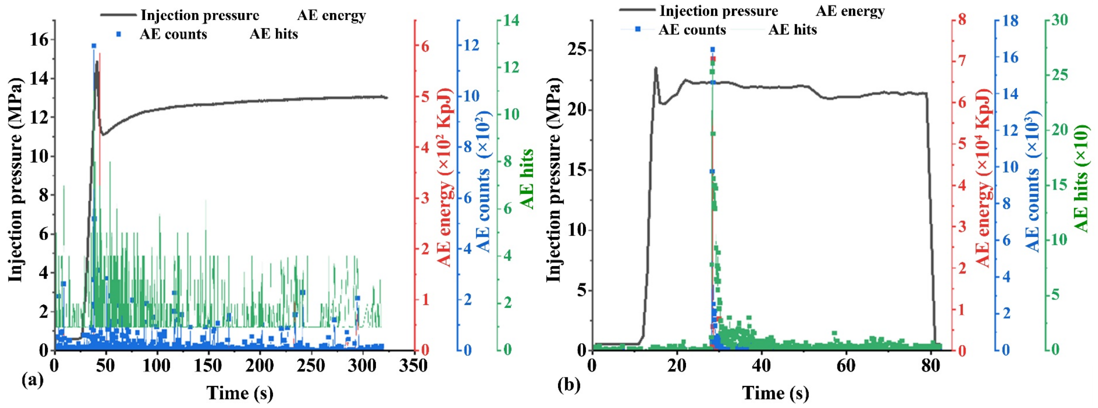

Figure 20. Pressure-time graph (a) C9 and (b) C8.

Figure 20 presents the injection pressure response for test C9, conducted at an intermediate injection rate of 5.0 ml/min—a rate chosen to bridge the gap between the optimal rate (2.2 mL/min) and previously observed high-rate behavior (8.0 mL/min). In this test, hydraulic fracture initiation (breakdown) occurred at 14.86 MPa, following the injection of 2.92 mL of fluid over 41 seconds. The peak pressure was sustained for merely 1 second, after which a rapid pressure drop to 11.11

MPa occurred within 6 seconds. Subsequently, the pressure stabilized at an average of 12.65 MPa. Acoustic emission (AE) data recorded minimal activity during the infiltration phase, suggesting limited microcrack nucleation and poor fracture complexity. This insufficient AE response indicates that the formation of branching or networked fractures was not favored at this rate. The results place 5.0 mL/min firmly within the high injection rate regime, which appears to surpass the optimal threshold for promoting energy-efficient, complex fracture propagation.

To further validate the negative impact of excessively high injection rates on fracture complexity, Test C8 was performed at a very high rate of 20 mL/min, also shown in Figure 20. A breakdown occurred rapidly at 23.54 MPa, with only 2.86 mL of fluid injected over 15 seconds. The system experienced an immediate pressure drop to 20.51 MPa within 2 seconds, followed by stabilization at an average of 18.19 MPa. AE monitoring during this test revealed extremely limited acoustic signals, signifying negligible fracture branching or microcrack coalescence. The abrupt and brief fluid-rock interaction period provided insufficient time for stress redistribution or the activation of multiple failure planes. This further substantiates that extremely high injection rates lead to localized, unstable fracturing that lacks spatial complexity, compromising the effectiveness of hydraulic fracturing in stimulating a productive reservoir.

Figure 21 highlights comparative tests conducted on sandstone (SST13) and bituminous coal (Coal14) to explore the material-dependent fracture behavior under similar injection conditions (2.2 mL/min). In test SST13, breakdown occurred at a notably high pressure of 30.01 MPa after the injection of 5.41 mL of fluid over 153 seconds. The pressure sharply declined to 22.05 MPa in 9 seconds, rebounded briefly to an average of 20.74 MPa, and eventually approached near-zero pressure. During fluid injection, AE sensors recorded only "hits" with no energy or count data, indicating a lack of distributed microcracking. These observations suggest that the tested sandstone was low-porosity and mechanically strong, consistent with its high Young's modulus. The sharp pressure decay after peak suggests the sudden creation of a single, dominant planar fracture, rather than the formation of a branched network.

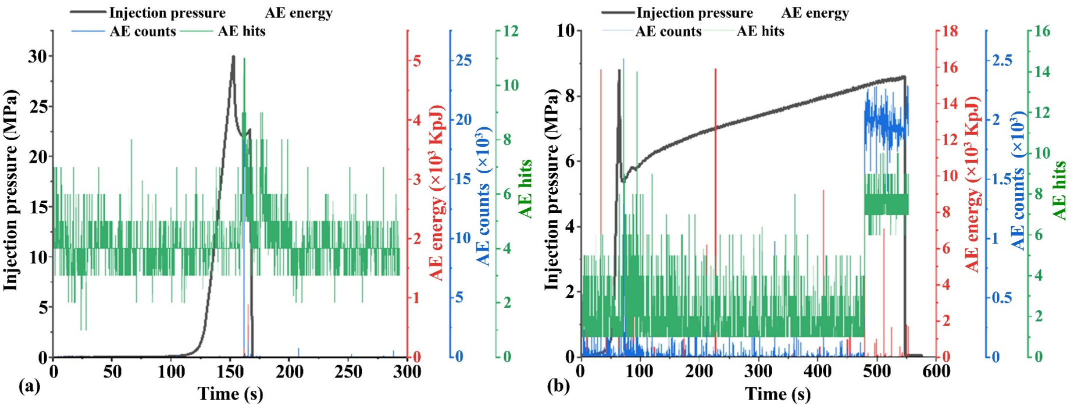

Figure 21. Pressure-time graph (a) SST13 and (b) Coal14.

In contrast, test Coal14, also illustrated in **Figure 21**, exhibited distinctly different behavior. Fracture initiation occurred at a low breakdown pressure of 8.79 MPa after 2.08 mL of fluid was injected over 64 seconds. Post-peak, the pressure dropped swiftly to 5.40 MPa within 9 seconds, then rose slightly to an average of 7.36 MPa, with no further breakdown events. The short infiltration time and low breakdown pressure are characteristic of coal's low tensile strength and low elastic modulus, which reduce its ability to resist deformation and sustain pressure. Unlike sandstone, AE monitoring during Coal14 revealed erratic but high-energy signals, indicative of brittle fracture processes and distributed microcracking common in cleated, anisotropic coal. These results emphasize the critical importance of lithological properties in determining the hydraulic fracture initiation and propagation mechanisms, underlining the need to customize injection strategies to match the mechanical behavior and internal fabric of the rock type.

3.3. Fracture Surface Morphology

To quantify the results of the fracture surface analysis, a 3D scanner, OKIO-H-2000, by TENYOUN, was used to measure and characterize the surface morphologies. The Surfer 21 software was then used to refine the surfaces and calculate the Joint Roughness Coefficient (JRC) value [34] Therefore, scanned 3D surfaces from the tested samples of C3, C10, C12, and SST13 are shown in **Figures 22-25**, along with their respective JRC numbers.

$$\text{JRC} = 32.2 + 32.47 \log Z_2 \tag{1}$$

$$Z_2 = \left[\frac{1}{(N-1)(X_{i+1} - X_i)^2} \sum_{i=1}^{N-1} (Z_{i+1} - Z_i)^2 \right]^{\frac{1}{2}} \tag{2}$$

where X_i is the coordinate of the surface profile parallel to the axial direction, Z_i is the height of the fracture surface profile, and N is the total number of data points of each profile. The fracture surface was divided into six groups, and the calculated JRC for each surface is the average of this group.

The Joint Roughness Coefficient (JRC) is a quantitative descriptor of fracture surface roughness and irregularity. Higher JRC values indicate more tortuous and uneven fracture surfaces, which may reflect enhanced fracture surface development and local fracture interactions during hydraulic fracturing. While JRC does not directly quantify fracture network complexity, it can provide supplementary insight into fracture surface characteristics associated with different injection conditions. In this study, sample C12 recorded the highest average JRC value of 23.89, indicating that it experienced the most complex fracture development among the selected specimens. This aligns with earlier findings that a 2.2 mL/min injection rate—used for C12—produced consistently optimal results, with favorable propagation behavior and a sufficient injection duration before breakdown. The high JRC supports the conclusion that moderate injection rates under suitable geological conditions promote complex fracture geometries.

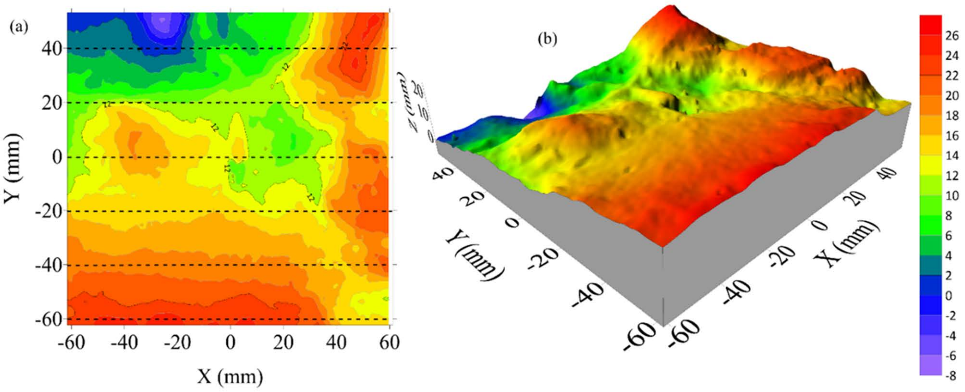

Figure 22. Scanned fracture surface: C3—Average JRC 14.97.

Sample C10, with an average JRC of 17.69, also demonstrated a relatively complex fracture surface, though not to the extent observed in C12. C10 was subjected to an intermediate injection rate within the transitional zone (1.0 - 1.9 mL/min), which was hypothesized to be near-optimal. The JRC value confirms that while C10 did not achieve the same level of complexity as C12, it still benefited from injection parameters that allowed for sustained pressure buildup and gradual fracture propagation. The moderate roughness observed in C10 suggests that, at this rate, the fluid was able to infiltrate natural weaknesses and microfractures in the rock mass, thereby enabling more irregular fracture formation.

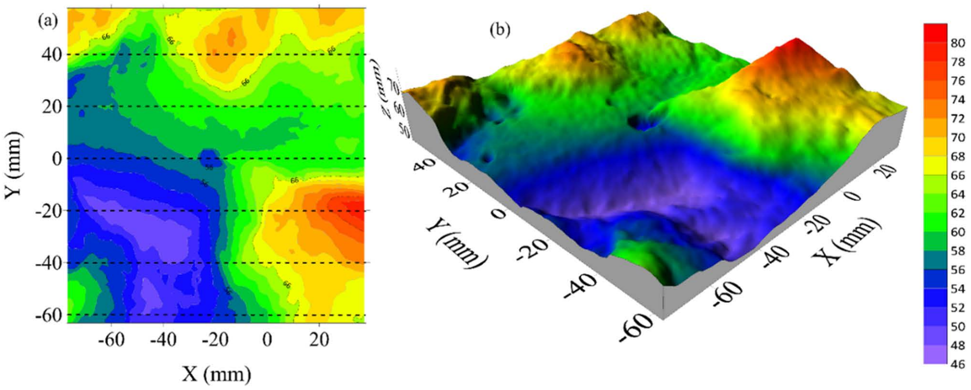

Figure 23. Scanned fracture surface: C10—Average JRC 17.69.

On the other end of the spectrum, sample C3, which was tested at a very low injection rate of 0.2 mL/min, had a significantly lower average JRC value of 14.97. This relatively smooth fracture surface indicates that the low injection rate failed to build sufficient pressure for the initiation of multiple fracture tips or significant propagation. The flat and uniform surface morphology associated with this sample supports the earlier conclusion that injection rates below a certain threshold do not provide the energy necessary for complex fracture formation. As such, C3 exemplifies the ineffective fracture behavior that arises when the pressure buildup is too gradual to initiate branching or irregular propagation paths.

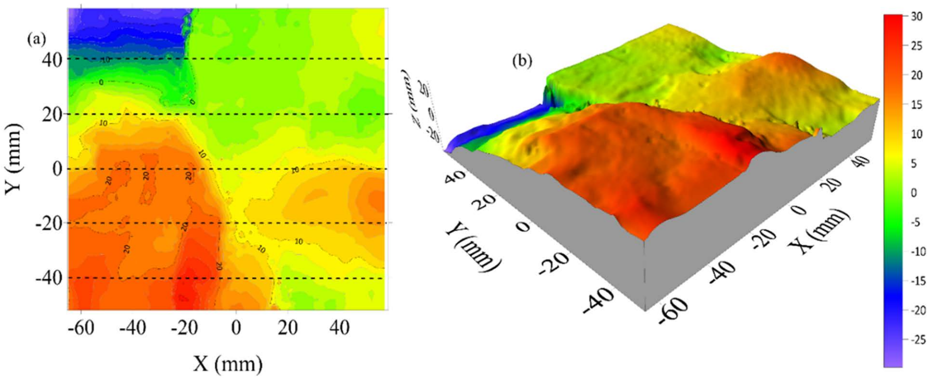

Figure 24. Scanned fracture surface: C12—Average JRC 23.89.

Sample SST13, a sandstone specimen, recorded an average JRC of 16.36, which is higher than C3 but still much lower than C12. Despite its longer injection duration (153 seconds), SST13 failed to produce a complex fracture network, primarily due to its low permeability and non-porous matrix. This inhibited fluid infiltration and limited the number of potential initiation points. The moderate JRC value reflects this outcome—while the fracture was not entirely smooth, the complexity was constrained by the rock's intrinsic properties. The pressure buildup led to a single dominant fracture rather than a branched network, confirming that rock lithology and permeability significantly influence the effectiveness of hydraulic fracturing, even when injection conditions are held constant.

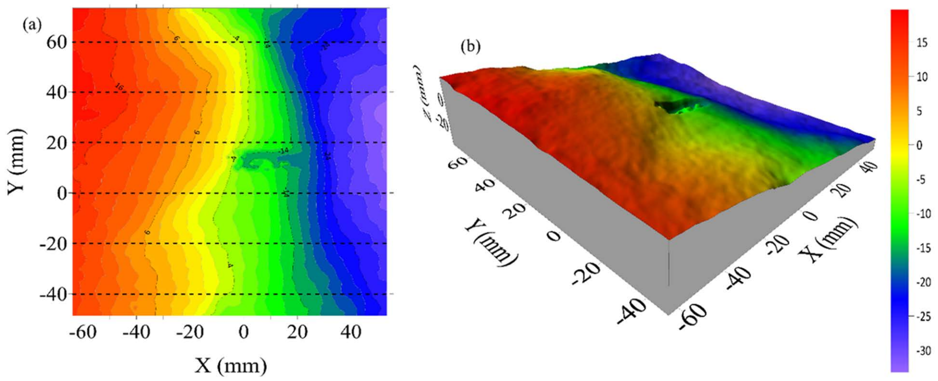

Figure 25. Scanned fracture surface: SST13—Average JRC 16.36.

3.4. Discussion

Table 3 below presents the results from all samples, highlighting the notable differences resulting from the various injection rates applied.

The results of this experimental study confirm that both extremely low and excessively high injection rates are ineffective in promoting the development of complex fracture networks during hydraulic fracturing. Tests conducted at very low rates, specifically below 0.2 mL/min, failed to generate sufficient injection pressure to induce tensile failure. For instance, Test C3, conducted at 0.2 mL/min, resulted in flat and planar fracture surfaces, indicating minimal branching or bifurcation of the fracture. Similarly, an increase to 0.6 mL/min still exhibited suboptimal fracturing behavior, suggesting insufficient pressure buildup to overcome the rock's tensile strength. Although Test C4 at 2.0 mL/min showed some promise in fracture complexity, the inconsistent result from Test C1, which was also conducted at the same rate, demonstrated the non-repeatability of performance at this level, thereby ruling it out as an optimal rate. These inconsistencies prompted further investigation within the intermediate injection rate range of 1.0 - 1.9 mL/min, where a progressive improvement in fracture complexity was observed. Notably, Test C10, conducted at 1.8 mL/min, displayed moderately favorable results and was thus selected to represent the transitional zone between ineffective and optimal injection conditions (see Figure 18).

Table 3. Test results: refer to Table 2 for experiment set conditions.

Test No.	Injected V. before initial Pb (mL)	Injection time before initial Pb (s)	Initial Pb (MPa)	Period of peak pressure (s)	Pressure recovery time (s)	Average pressure after recovery (MPa)
C1	4.96	149	30.44	8	15	27.70
C2	7.68	41	29.82	1	5	26.29
C3	4.33	1612	29.68	3	76	27.78
C4	3.38	107	18.51	101	16	19.79
C5	2.95	31	15.89	1	3	12.38
C6	2.72	301	21.8	1	26	17.80
C7	2.55	27	24.01	1	7	21.69
C8	2.86	15	23.54	1	2	18.19
C9	2.92	41	14.86	1	6	12.65
C10	2.67	94	17.4	1	14	15.95
C11	11.48	319	7.61	9	48	8.22
C12	16.86	460	17.44	1	29	16.86
SST13	5.41	153	30.01	1	9	20.74
Coal14	2.08	64	8.79	1	6	7.36
Coal15	3.45	210	-	-	-	-

To identify a more consistent injection rate capable of yielding complex fractures, the injection rate was increased to 2.2 mL/min, which was tested in three separate trials. Among these, Tests C11 and C12 both consistently demonstrated enhanced fracture complexity and energy release patterns, supported by Acoustic Emission (AE) data and pressure-time curves. In particular, Figure 19(a) (C11) illustrates a stable and prolonged propagation pressure phase, characterized by a horizontal inflection on the pressure curve—indicative of sustained crack growth and resistance to sudden breakdown. This behavior is typically associated with stable fracture propagation and network development, as opposed to abrupt failure. The consistency of these results confirmed that 2.2 mL/min falls within the optimal injection range. The enhanced fracture geometry at this rate is attributed to the favorable balance between pressure build-up and rock resistance, enabling more uniform energy dissipation and complex fracture nucleation.

To assess the upper boundary of the optimal injection rate range, a test was performed at 5.0 mL/min (Test C9). Although the breakdown pressure was successfully reached, the subsequent AE signals and fracture morphology (shown in **Figure 12**) indicated limited microcracking activity and low fracture complexity. The short duration between fluid injection and failure suggested that the system lacked sufficient time for distributed microcrack growth, resulting instead in the formation of a dominant, planar fracture. To further verify the adverse effects of high-rate injection, an extreme case was tested at 20 mL/min (Test C8). This trial exhibited an instantaneous pressure drop and minimal AE activity, indicating brittle, uncontrolled fracture propagation with no evidence of branching. The fracture surfaces were similarly flat and indicative of a single propagation front, confirming that excessively high injection rates lead to rapid energy release and suppress the development of intricate fracture systems (refer to **Figure 12**).

Based on the collected data and fracture characterization across the full injection rate spectrum, the study identified three distinct operational regimes: (i) a low-rate regime (<1.0 mL/min), which produced planar and simplistic fractures due to insufficient pressure and energy, (ii) an optimal-rate regime (centered around 2.2 mL/min), which promoted gradual pressurization, enhanced AE activity, and complex fracture branching, and (iii) a high-rate regime (≥5.0 mL/min), where rapid pressure surges caused early failure with limited fracture network development. These findings are conceptually illustrated in **Figure 26**, which delineates the relationship between injection rate and fracture complexity. The figure further emphasizes that successful hydraulic fracturing in low-permeability rock masses is highly sensitive to the control of injection parameters. The identification of these regimes offers critical insight for optimizing fracturing strategies in field operations, particularly when targeting anisotropic and heterogeneous rock formations.

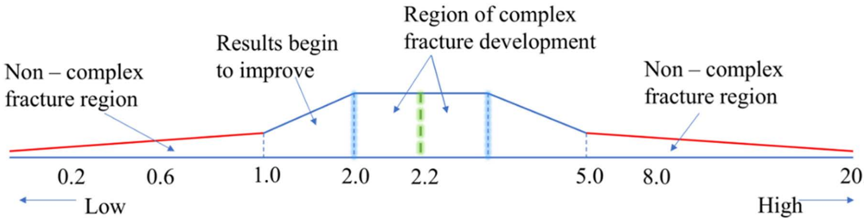

Figure 26. Spectrum of injection rates (mL/min) falling under poor and optimal regions.

The histograms in **Figures 27-29** highlight the various corresponding results parameters for the respective injection rates in the three material types ([C5, C6, C10, C12], SST13, Coal14 representing concrete, sandstone and coal, respectively), with the injection rate labeled as Q and the injected fluid volume before initial breakdown as Inj. Vol., period of fluid injection before initial breakdown pressure as t, initial breakdown pressure as Pb, period of peak pressure as Pp, pressure recovery time as Pr, and average pressure after recovery (without further breakdown) as Pav. The graphs show that an optimum injection rate will have an extended period of fluid injection accompanied by a consistent AE energy before initial breakdown occurs, which indicates that multiple fracture initiation points are being formed.

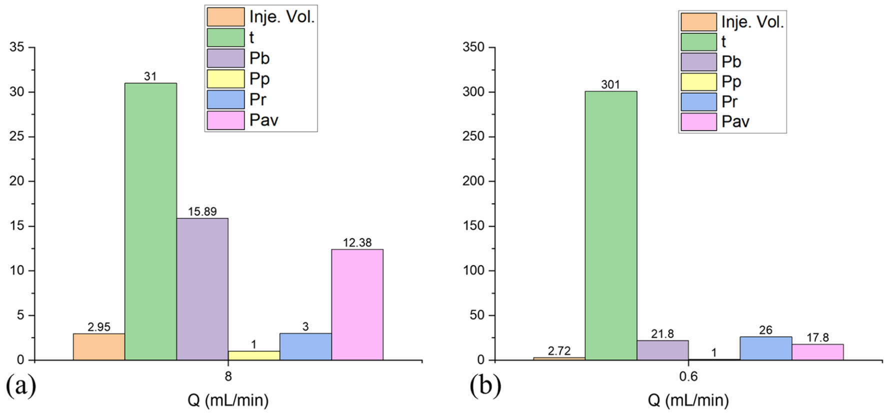

Figure 27. Fluid infiltration time - injection rate (a) C5, (b) C6.

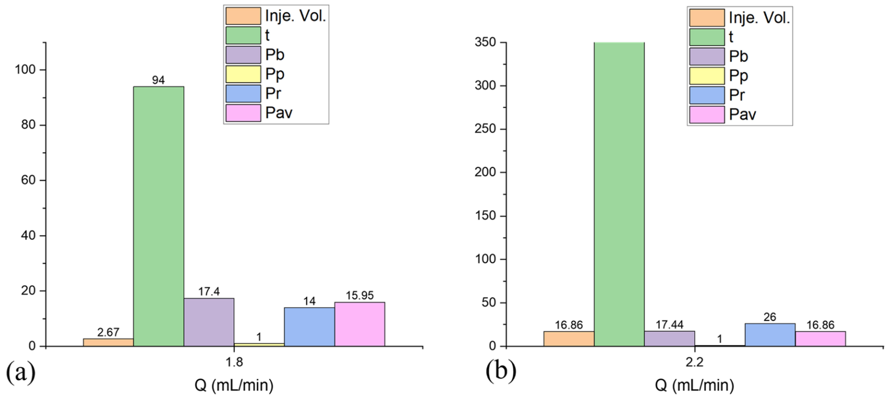

Figure 28. Fluid infiltration time - injection rate (a) C10, (b) C12.

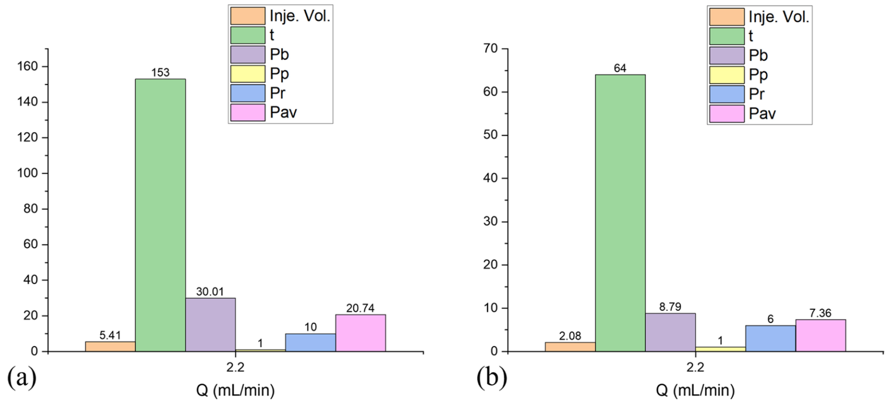

Figure 29. Fluid infiltration time - injection rate (a) SST13, (b) Coal14.

4. Conclusions

This study systematically investigated the influence of fluid injection rate on fracture complexity during hydraulic fracturing in various rock samples, utilizing specimens made from bituminous coal, sandstone, and concrete with standardized dimensions. Both qualitative observations and quantitative data, including pressure curves, fracture morphology, and acoustic emission responses, were integrated to establish optimal injection conditions for maximizing the development of the fracture network. Considering these, the following conclusions can be drawn:

1. The experimental results clearly delineated three injection rate regimes. In the low-rate region (<1.0 mL/min), the fluid injection was insufficient to sustain propagation pressure once breakdown occurred; the sudden drop in pressure led to single fracture development, as in the case of C3. C4 conducted with 2.0 mL/min had potential for optimal results, but lacked consistency; this can be seen from a different pressure evolution and a flat fracture surface on the tested sample for C1. Similarly, the high-rate region (≥5.0 mL/min) led to sudden pressure surges, characterized by instantaneous failure, reduced AE activity, and a lack of fracture complexity. The fractures here were also planar, indicating that rapid energy release inhibited the growth of distributed microcracks.
2. In the intermediate or optimal injection rate range, particularly at 2.2 mL/min, fractures exhibited significantly higher complexity. All samples in this group show consistent AE patterns and complex fracture networks, except sandstone and coal.
3. Based on the fracture surface analysis and pressure evolution data, below 0.2 mL/min, fracture initiation was not achieved; 0.2 mL/min is thus defined as the minimum effective injection rate. 1.0 - 1.9 mL/min represents a transitional zone with increasing fracture complexity, while at a rate of 2.0 mL/min, optimal results were observed but lacked repeatable optimization. 5.0 mL/min and 20 mL/min produced simple, planar fractures, demonstrating that high injection rates result in rapid pressure drops and uncontrolled failure.
4. Fracture complexity was found to correlate strongly with the shape of the pressure-time curve, particularly the presence of horizontal inflection points and longer stable propagation phases. Water as a fracturing fluid does not permit effective optimization of the injection rate in non-porous, highly impermeable, or low-tensile-strength brittle rock types (due to a shorter elastic region, which will not support a prolonged fluid infiltration time critical for forming multiple fracture initiation points). Nevertheless, it may be applicable in moderately permeable rock formations where fluid infiltration can facilitate fracture complexity.

Generally, the study confirms that fracture complexity is highly sensitive to injection rate and that optimizing this parameter is essential to achieving desirable fracturing outcomes in anisotropic rocks. The identification of distinct operational regimes, including simple fractures at low and high rates, and complex fractures in the optimal range, provides valuable guidance for designing hydraulic fracturing protocols in both laboratory and field-scale applications. This work offers a foundational reference for future research and practical implementation in unconventional reservoir stimulation. Future work should incorporate larger sample sizes, CT-based internal fracture mapping, permeability tests of the samples for more accurate results, and refined stress conditions to enhance fracture propagation and network complexity. Under the present laboratory conditions, concrete was used as a surrogate material because of its relatively homogeneous composition and controllable mechanical properties, which make it suitable for simulating rock-like mechanical behavior. Based on the tested concrete specimens, an injection rate of 2.2 mL/min was identified as optimal; however, similar behavior was not consistently observed in coal and sandstone, and therefore, this value should not be interpreted as a universal optimum across different materials.

CRediT

Authorship contribution statement: Tresphord Chishimba: Writing—original draft, Methodology, Conceptualization. **Weiguo Liang**: Supervision, Conceptualization, **Ngambua Ngambua Rene**: Writing—review & editing, Software, Project administration, Data curation; **Irfan Ahmad Butt**: Writing—review & editing.

Data Availability

Data will be made available on request.

Acknowledgements

This work was supported by the National Natural Science Foundation of China (No. 51874206, No. 52274222), Key Projects of National Joint Fund for Regional Innovation and Development (U22A20167) and the Science and Technology Major Project in Shanxi Province (20201102002), which is gratefully acknowledged.

Conflicts of Interest

The authors declare that they have no known competing financial interests or personal relationships that could have appeared to influence the work reported in this paper.

References

[1] Yu, H., Xu, W., Li, B., Huang, H., Micheal, M., Wang, Q., *et al.* (2023) Hydraulic Fracturing and Enhanced Recovery in Shale Reservoirs: Theoretical Analysis to Engineering Applications. *Energy & Fuels*, **37**, 9956-9997. https://doi.org/10.1021/acs.energyfuels.3c01029

[2] Mwakipunda, G.C., Wang, Y., Mgimba, M.M., Ngata, M.R., Alhassan, J., Mkono, C.N., *et al.* (2023) Recent Advances in Carbon Dioxide Sequestration in Deep Unmineable Coal Seams Using CO_2-ECBM Technology: Experimental Studies, Simulation, and Field Applications. *Energy & Fuels*, **37**, 17161-17186.

https://doi.org/10.1021/acs.energyfuels.3c03004

[3] Guanhua, N., Kai, D., Shang, L. and Qian, S. (2019) Gas Desorption Characteristics Effected by the Pulsating Hydraulic Fracturing in Coal. *Fuel*, **236**, 190-200. https://doi.org/10.1016/j.fuel.2018.09.005

[4] Ji, Y., Zhuang, L., Wu, W., Hofmann, H., Zang, A. and Zimmermann, G. (2021) Cyclic Water Injection Potentially Mitigates Seismic Risks by Promoting Slow and Stable Slip of a Natural Fracture in Granite. *Rock Mechanics and Rock Engineering*, **54**, 5389-5405. https://doi.org/10.1007/s00603-021-02438-7

[5] Wu, K., Paranjothi, G., Milford, J.B. and Kreith, F. (2016) Transition to Sustainability with Natural Gas from Fracking. *Sustainable Energy Technologies and Assessments*, **14**, 26-34. https://doi.org/10.1016/j.seta.2016.01.003

[6] Kong, L., Ranjith, P.G. and Li, B.Q. (2021) Fluid-Driven Micro-Cracking Behaviour of Crystalline Rock Using a Coupled Hydro-Grain-Based Discrete Element Method. *International Journal of Rock Mechanics and Mining Sciences*, **144**, Article 104766. https://doi.org/10.1016/j.ijrmms.2021.104766

[7] Zhang, B., Cui, X., Wang, L. and Fu, X. (2022) Rock Fracture Response Exposed to Hydraulic Fracturing: Insight into the Effect of Injection Rate on Aperture Pattern. *Advances in Materials Science and Engineering*, **2022**, 1-7. https://doi.org/10.1155/2022/9431143

[8] Zhou, X. and Burbey, T.J. (2013) Fluid Effect on Hydraulic Fracture Propagation Behavior: A Comparison between Water and Supercritical CO_2-Like Fluid. *Geofluids*, **14**, 174-188. https://doi.org/10.1111/gfl.12061

[9] Zhang, X., Zhang, Y. and Huang, B. (2021) Investigation of the Fracturing Effect Induced by the Disturbing Stress of Hydrofracturing Using the Bonded-Particle Model. *Geofluids*, **2021**, 1-24. https://doi.org/10.1155/2021/9988748

[10] Irwin, G.R. (1957) Analysis of Stresses and Strains near the End of a Crack Traversing a Plate. *Journal of Applied Mechanics*, **24**, 361-364. https://doi.org/10.1115/1.4011547

[11] Griffith, A.A. (1921) The Phenomena of Rupture and Flow in Solids. *Philosophical Transactions of the Royal Society of London, Series A, Containing Papers of a Mathematical or Physical Character*, **221**, 163198.

[12] Roylance, D. (2001) Introduction to Fracture Mechanics. https://live.ocw.mit.edu/courses/3-91-mechanical-behavior-of-plastics-spring-2007/ca3759efc1b8fd66d57dce1147d4a1db_23_frac.pdf

[13] Zeng, X. and Wei, Y. (2017) Crack Deflection in Brittle Media with Heterogeneous Interfaces and Its Application in Shale Fracking. *Journal of the Mechanics and Physics of Solids*, **101**, 235-249. https://doi.org/10.1016/j.jmps.2016.12.012

[14] Xi, X., Shipton, Z.K., Kendrick, J.E., Fraser-Harris, A., Mouli-Castillo, J., Edlmann, K., *et al.* (2022) Mixed-Mode Fracture Modelling of the Near-Wellbore Interaction between Hydraulic Fracture and Natural Fracture. *Rock Mechanics and Rock Engineering*, **55**, 5433-5452. https://doi.org/10.1007/s00603-022-02922-8

[15] Kolawole, O. and Ispas, I. (2020) Interaction between Hydraulic Fractures and Natural Fractures: Current Status and Prospective Directions. *Journal of Petroleum Exploration and Production Technology*, **10**, 1613-1634. https://doi.org/10.1007/s13202-019-00778-3

[16] Dehghan, A.N. (2020) An Experimental Investigation into the Influence of Pre-Existing Natural Fracture on the Behavior and Length of Propagating Hydraulic Fracture. *Engineering Fracture Mechanics*, **240**, Article 107330. https://doi.org/10.1016/j.engfracmech.2020.107330

[17] Zheng, Y., Liu, J. and Zhang, B. (2019) An Investigation into the Effects of Weak Interfaces on Fracture Height Containment in Hydraulic Fracturing. *Energies*, **12**, Article 3245. https://doi.org/10.3390/en12173245

[18] Ma, Y., Wang, D. and Zheng, Y. (2023) Influence of the Bedding Plane on the Propagation of Multiple Hydraulic Fractures. *Frontiers in Earth Science*, **10**, Article 1077652. https://doi.org/10.3389/feart.2022.1077652

[19] Ishida, T., Chen, Q., Mizuta, Y. and Roegiers, J. (2004) Influence of Fluid Viscosity on the Hydraulic Fracturing Mechanism. *Journal of Energy Resources Technology*, **126**, 190-200. https://doi.org/10.1115/1.1791651

[20] Zheng, Y., Wei, H., Zhang, A. and Niu, Q. (2025) Exploring the Influence of Fluid Viscosity on the Hydraulic Fracture Propagation in Composite Coal Seams. *Engineering Fracture Mechanics*, **323**, Article 111203. https://doi.org/10.1016/j.engfracmech.2025.111203

[21] Brady, B.H. and Brown, E.T. (2006) Rock Mechanics: For Underground Mining. Springer Science & Business Media.

[22] Lockner, D. (1993) The Role of Acoustic Emission in the Study of Rock Fracture. *International Journal of Rock Mechanics and Mining Sciences & Geomechanics Abstracts*, **30**, 883-899. https://doi.org/10.1016/0148-9062(93)90041-b

[23] Heinze, T., Galvan, B. and Miller, S.A. (2015) Modeling Porous Rock Fracturing Induced by Fluid Injection. *International Journal of Rock Mechanics and Mining Sciences*, **77**, 133-141. https://doi.org/10.1016/j.ijrmms.2015.04.003

[24] Zoback, M.D. and Kohli, A.H. (2019) Unconventional Reservoir Geomechanics. Cambridge University Press. https://doi.org/10.1017/9781316091869

[25] Hubbert, M.K. and Willis, D.G. (1957) Mechanics of Hydraulic Fracturing. *Transactions of the AIME*, **210**, 153-168. https://doi.org/10.2118/686-g

[26] Singh, S.B., Munjal, P. and Thammishetti, N. (2015) Role of Water/Cement Ratio on Strength Development of Cement Mortar. *Journal of Building Engineering*, **4**, 94-100. https://doi.org/10.1016/j.jobe.2015.09.003

[27] Li, W. (2021) Analysis of the Influence of Water-Cement Ratio on Concrete Strength. *E3S Web of Conferences*, **283**, Article 301016. https://doi.org/10.1051/e3sconf/202128301016

[28] Bieniawski, Z.T. and Bernede, M.J. (1979) Suggested Methods for Determining the Uniaxial Compressive Strength and Deformability of Rock Materials. *International Journal of Rock Mechanics and Mining Sciences & Geomechanics Abstracts*, **16**, 137. https://doi.org/10.1016/0148-9062(79)91450-5

[29] Pawar, Y. and Kate, S. (2020) Curing of Concrete: A Review. *International Journal of Engineering Research & Technology*, **7**, 1820-1824. https://www.academia.edu/download/64721827/IRJET_V7I8302.pdf

[30] Tan, K. and Gjorv, O.E. (1996) Performance of Concrete under Different Curing Conditions. *Cement and Concrete Research*, **26**, 355-361. https://doi.org/10.1016/s0008-8846(96)85023-x

[31] Xiu, Z., Wang, S., Ji, Y., Wang, F., Ren, F. and Nguyen, V. (2021) Loading Rate Effect on the Uniaxial Compressive Strength (UCS) Behavior of Cemented Paste Backfill (CPB). *Construction and Building Materials*, **271**, Article 121526. https://doi.org/10.1016/j.conbuildmat.2020.121526

[32] Neville, A.M. (1995) Properties of Concrete. Vol. 4. Longman London.

[33] Speight, J.G. (2012) The Chemistry and Technology of Coal. CRC Press.

https://books.google.com/books?hl=en&lr=&id=UWAWLUk4nJIC&oi=fnd&pg=PP1&dq=Speight,+J.G.,+The+chemistry+and+technology+of+coal.+2012:+CRC+press.&ots=X1dwtPGCGU&sig=tMWnsi_Jzk7ZCXG8Kbk7Fjx75GQ

[34] Tse, R. and Cruden, D.M. (1979) Estimating Joint Roughness Coefficients. *International Journal of Rock Mechanics and Mining Sciences & Geomechanics Abstracts*, **16**, 303-307. https://doi.org/10.1016/0148-9062(79)90241-9